Transition Phenomena in Turbulent Natural Convective Flow Using Subgrid Modeling

***G.H. Yeoh[1,2], G.E. Lau [1], V. Timchenko [1] and J.A. Reizes [1]**

[1]School of Mechanical and Manufacturing Engineering, University of New South Wales, Sydney, NSW 2052, Australia.
[2]Australian Nuclear Science and Technology Organisation (ANSTO), PMB 1, Menai, NSW 2234, Australia.

*Corresponding author: g.yeoh@UNSW.EDU.AU

Abstract

Turbulent natural convection in an enclosed cavity with two differentially heated opposite walls is investigated numerically by means of large-eddy simulation (LES). The dynamic global-coefficient subgrid-scale (SGS) model based on the "global equilibrium" approach for weakly compressible flows is applied. It can be shown that the physical mechanisms of the transition phenomena could be adequately captured. Tollmien-Schlichting waves persist along the hot and cold vertical walls. Nevertheless, the onset of transition occurs much earlier along the hot vertical wall in comparison to the cold vertical wall. Relaminarization flow regimes along the horizontal adiabatic top and bottom walls have been found to be distinctly different.

Keywords: Transition phenomena, turbulent natural convective flow, large eddy simulation, dynamic global model.

Introduction

Turbulent natural convection in tall cavities with two differentially heated opposite walls has been the subject of numerous numerical studies due to its wide application in diverse industries. For example, cooling of electronic components or solar energy applications. In such configurations, two distinct patterns are usually observed in the flow structure – the boundary layers along the walls and the recirculating motion in the core. As succinctly indicated by Paolucci and Chenoweth (1989), the transition from a laminar to turbulent flow occurs at the critical Rayleigh number between 10^7 and 10^8. A further increase in the Rayleigh number leads to a highly-turbulent motion in which wave-like structures may be found in the boundary layers (Paolucci, 1990, Trias et al., 2007).

One important feature of a buoyant flow in a tall cavity is the concurrent occurrence of laminar, transitional and turbulent regimes along the vertical walls as pointed out by Betts and Bokhari (2000) who have performed a number of experiments to investigate the buoyancy-driven flow in a rectangular cavity with an aspect ratio of 28. It was shown that the flow became fully turbulent in the downstream edges along both the heated and cooled vertical walls. Physical mechanisms involved in the transition process have been detailed by Paolucci (1990). Travelling waves in the distinctive "hook" pattern have been found to precede the transition process; a finding consistent with a number of experimental studies by Elder (1965) and Jaluria and Gebhart (1977). These characteristic folding waves have been found to closely resemble the Tollmien-Schlichting waves in forced convection boundary layers.

In this present study, the transition phenomena of turbulent natural convection in a tall cavity is elucidated via the consideration of the LES and SGS modeling of the dynamic procedure based on

"global equilibrium". The concurrent occurrence of laminar, transitional and turbulent regimes along the vertical walls and relaminarization regimes along the horizontal walls are discussed.

Mathematical Formulation

Governing Equations

In LES, scale separation between large-scale structures and small-scale eddies can be achieved by spatially filtering the conservation equations of the mass, momentum and energy which in the present case are assumed to have variable transport properties. Adopting Favre averaging and neglecting acoustic waves, the fluid motion can be described by the filtered continuity, momentum, and energy equations for a weakly compressible flow as

$$\frac{\partial \bar{\rho}}{\partial t} + \frac{\partial \left(\bar{\rho} \tilde{u}_j \right)}{\partial x_j} = 0 \tag{1}$$

$$\frac{\partial \left(\bar{\rho} \tilde{u}_j \right)}{\partial t} + \frac{\partial \left(\bar{\rho} \tilde{u}_i \tilde{u}_j \right)}{\partial x_i} = -\frac{\partial \bar{p}}{\partial x_j} + \frac{\partial \tilde{\sigma}_{ij}}{\partial x_i} - \frac{\partial \tau_{ij}}{\partial x_i} + \left(\bar{\rho} - \rho_{ref} \right) g_i \tag{2}$$

$$\frac{\partial \left(C_p \bar{\rho} \tilde{T} \right)}{\partial t} + \frac{\partial \left(C_p \bar{\rho} \tilde{u}_i \tilde{T} \right)}{\partial x_i} = \frac{\partial}{\partial x_i} \left(\frac{\mu C_p}{Pr} \frac{\partial \tilde{T}}{\partial x_i} \right) - \frac{\partial h_i}{\partial x_i} \tag{3}$$

where $\bar{\rho}$ and $\tilde{T}$ are the filtered density and temperature respectively, ρ_{ref} is the reference density at reference temperature T_{ref}, $\tilde{u}_i$ and g_i are the respective filtered velocity and gravitational vectors, $\bar{p}$ is the filtered pressure, *Pr* is the Prandtl number and μ is the dynamic viscosity.

In Eq. (2), $\tilde{\sigma}_{ij}$ is determined by the Stoke's hypothesis as

$$\tilde{\sigma}_{ij} = \mu(T) \left(\frac{\partial \tilde{u}_i}{\partial x_j} + \frac{\partial \tilde{u}_j}{\partial x_i} \right) - \frac{2}{3} \mu(T) \frac{\partial \tilde{u}_k}{\partial x_k} \tag{4}$$

while the dynamic viscosity in Eq. (3) is calculated according to

$$\mu = 18.27 \times 10^{-6} \frac{291.15 + C}{\tilde{T} + C} \left(\frac{\tilde{T}}{291.15} \right)^{3/2} \tag{5}$$

where *C* is the Sutherland constant. For air, *C* and *Pr* are 120 and 0.71 respectively. The unresolved turbulent SGS momentum stress tensor $\tau_{ij} = \bar{\rho} \left(u_i u_j - \tilde{u}_i \tilde{u}_j \right)$ in Eq. (2) is modelled through an SGS-viscosity model as

$$\tau_{ij} - \frac{1}{3} \tau_{kk} \delta_{ij} = -2 \mu_{sgs} \left(\tilde{S}_{ij} - \frac{1}{3} \tilde{S}_{kk} \delta_{ij} \right) \tag{6}$$

where μ_{sgs} is the SGS viscosity and $\tilde{S}_{ij} = \left(\partial \tilde{u}_i / \partial x_j + \partial \tilde{u}_j / \partial x_i \right) / 2$. As detailed by Erlebacher et al. (1992), τ_{kk} is assumed to be negligible for natural convective flows in which the effect of acoustic waves is considered to be small. The SGS thermal flux vector h_i is modelled by the SGS Prandtl number Pr_{sgs} as outlined by Eidson (1985):

$$h_i = \bar{\rho}\left(u_i T - \tilde{u}_i \tilde{T}\right) \approx -\frac{\mu_{sgs}}{Pr_{sgs}} \frac{\partial \tilde{T}}{\partial x_i} \tag{7}$$

It is noted that variation of the SGS thermal flux as represented by Eq. (7) accounts for variable thermal diffusion due to changing SGS viscosity.

Dynamic Model Based on Global Equilibrium

The dynamic global-coefficient model proposed by You and Moin (2007) which is based on "global equilibrium" between the SGS dissipation and viscous dissipation requires only a single-level test filtering procedure. In formulating this model, the test-filtered resolved-scale turbulent kinetic energy equation can be obtained as Subtracting test-filtered resolved-scale turbulent kinetic energy equation from the test-filtered total turbulent kinetic energy equation yields a transport equation for $T_{ii} = \hat{\bar{\rho}}\widehat{u_i u_i} - \hat{\bar{\rho}}\hat{\bar{u}}_i\hat{\bar{u}}_i$ and invoking the Germano identity, a transport equation for $L_{ii} = T_{ii} - \hat{\tau}_{ii}$ is derived as

$$\begin{aligned}
\underbrace{\frac{\partial\left(\hat{\bar{\rho}}\tilde{u}_i\tilde{u}_i - \hat{\bar{\rho}}\hat{\tilde{u}}_i\hat{\tilde{u}}_i\right)}{\partial t}}_{\text{time variation}} = \frac{\partial}{\partial x_j}\Bigg\{ & -\left(\hat{\bar{\rho}}\tilde{u}_i\tilde{u}_i\tilde{u}_j - \hat{\bar{\rho}}\hat{\tilde{u}}_i\hat{\tilde{u}}_i\hat{\tilde{u}}_j\right) - 2\left(\bar{p}\tilde{u}_j - \hat{\bar{p}}\hat{\tilde{u}}_j\right) \\
& + 2\mu\Bigg[\left(\tilde{u}_i\frac{\partial\tilde{u}_i}{\partial x_j} - \hat{\tilde{u}}_i\frac{\partial\hat{\tilde{u}}_i}{\partial x_j}\right) + \left(\tilde{u}_i\frac{\partial\tilde{u}_j}{\partial x_i} - \hat{\tilde{u}}_i\frac{\partial\hat{\tilde{u}}_j}{\partial x_i}\right) \\
& - \frac{2}{3}\left(\widehat{\tilde{u}_i\frac{\partial\tilde{u}_k}{\partial x_k}} - \hat{\tilde{u}}_i\frac{\partial\hat{\tilde{u}}_k}{\partial x_k}\right)\delta_{ij}\Bigg] - 2\left(\widehat{\tilde{u}_i\tau_{ij}} - \hat{\tilde{u}}_i T_{ij}\right)\Bigg\} \\
& + 2\underbrace{\left(\widehat{\bar{p}\frac{\partial\tilde{u}_k}{\partial x_k}} - \hat{\bar{p}}\frac{\partial\hat{\tilde{u}}_k}{\partial x_k}\right)}_{\text{pressure dilatation}} \\
& - 2\mu\Bigg[\left(\widehat{\frac{\partial\tilde{u}_i}{\partial x_j}\frac{\partial\tilde{u}_i}{\partial x_j}} - \frac{\partial\hat{\tilde{u}}_i}{\partial x_j}\frac{\partial\hat{\tilde{u}}_i}{\partial x_j}\right) + \left(\widehat{\frac{\partial\tilde{u}_i}{\partial x_j}\frac{\partial\tilde{u}_j}{\partial x_i}} - \frac{\partial\hat{\tilde{u}}_i}{\partial x_j}\frac{\partial\hat{\tilde{u}}_j}{\partial x_i}\right) \\
& - \frac{2}{3}\left(\widehat{\frac{\partial\tilde{u}_i}{\partial x_i}\frac{\partial\tilde{u}_k}{\partial x_k}} - \frac{\partial\hat{\tilde{u}}_i}{\partial x_i}\frac{\partial\hat{\tilde{u}}_k}{\partial x_k}\right)\delta_{ij}\Bigg] + 2\left(\widehat{\tau_{ij}\tilde{S}_{ij}} - T_{ij}\hat{\tilde{S}}_{ij}\right)
\end{aligned} \tag{9}$$

For a weakly compressible flow, the pressure dilatation term in Eq. (9) can be neglected following the observation of Vreman et al. (1995). Also, as detailed by Lee et al. (2010), the time variation term can be taken to be negligible in statistically steady turbulent flows. By taking volume averaging of Eq. (9) and assuming "global equilibrium", the model coefficient C_{DVME} can be obtained as

$$C_{DVME} = -\frac{\left\langle \mu\left[\left(\alpha_{ij}\alpha_{ij} - \hat{\tilde{\alpha}}_{ij}\hat{\tilde{\alpha}}_{ij}\right) + \left(\alpha_{ij}\alpha_{ji} - \hat{\tilde{\alpha}}_{ij}\hat{\tilde{\alpha}}_{ji}\right) - \tfrac{2}{3}\left(\alpha_{ii}\alpha_{kk} - \hat{\tilde{\alpha}}_{ii}\hat{\tilde{\alpha}}_{kk}\right)\delta_{ij}\right]\right\rangle_V}{2\left\langle \bar{\rho}\Pi^g\tilde{S}_{ij}\tilde{S}_{ij} - \hat{\bar{\rho}}\Pi^t\hat{\tilde{S}}_{ij}\hat{\tilde{S}}_{ij}\right\rangle_V} \tag{10}$$

The SGS Prandtl number could also be determined dynamically using the "global equilibrium" hypothesis. Subtracting the transport equation for the Favre-filtered resolved temperature variance

from the Favre-filtered total temperature variance equation and the test-filtered transport equation for resolved temperature variance from test-filtered total temperature variance equation results in the transport equations for $\theta_j = \bar{\rho}\left(TT - \tilde{T}\tilde{T}\right)$ and $\Theta_j = \bar{\rho}\tilde{T}\tilde{T} - \hat{\bar{\rho}}\hat{\tilde{T}}\hat{\tilde{T}}$ which they can be expressed as

$$\begin{aligned}\frac{\partial}{\partial t}\left(C_p\theta_j\right) = \frac{\partial}{\partial x_j}\Bigg[& -C_p\left(\bar{\rho}u_jTT - \bar{\rho}\tilde{u}_j\tilde{T}\tilde{T}\right) + 2\left(\overline{kT\frac{\partial T}{\partial x_j}} - \tilde{k}\tilde{T}\frac{\partial \tilde{T}}{\partial x_j}\right) + 2C_p\tilde{T}q_j\Bigg] \\ & -2\left(\overline{k\frac{\partial T}{\partial x_j}\frac{\partial T}{\partial x_j}} - \tilde{k}\frac{\partial \tilde{T}}{\partial x_j}\frac{\partial \tilde{T}}{\partial x_j}\right) - 2C_pq_j\frac{\partial \tilde{T}}{\partial x_j}\end{aligned} \tag{11}$$

$$\begin{aligned}\frac{\partial}{\partial t}\left(C_p\Theta_j\right) = \frac{\partial}{\partial x_j}\Bigg\{ & -C_p\left(\bar{\rho}u_jTT - \hat{\bar{\rho}}\hat{\tilde{u}}_j\hat{\tilde{T}}\hat{\tilde{T}}\right) + 2\left(\overline{kT\frac{\partial T}{\partial x_j}} - \hat{\tilde{k}}\hat{\tilde{T}}\frac{\partial \hat{\tilde{T}}}{\partial x_j}\right) + 2C_pQ_j\hat{\tilde{T}}\Bigg\} \\ & -2k\left(\overline{\frac{\partial T}{\partial x_j}\frac{\partial T}{\partial x_j}} - \frac{\partial \hat{\tilde{T}}}{\partial x_j}\frac{\partial \hat{\tilde{T}}}{\partial x_j}\right) - 2C_pQ_j\frac{\partial \hat{\tilde{T}}}{\partial x_j}\end{aligned} \tag{12}$$

where

$$q_j = -\frac{\mu_{sgs}}{Pr_{sgs}}\frac{\partial \tilde{T}}{\partial x_j} \tag{13}$$

$$Q_j = -\frac{\mu^t_{sgs}}{Pr_{sgs}}\frac{\partial \hat{\tilde{T}}}{\partial x_j} \tag{14}$$

The transport equation for $\mathcal{L}^{\theta}_j = \Theta - \hat{\theta}$ is derived as

$$\begin{aligned}\underbrace{\frac{\partial}{\partial t}\left(C_p\mathcal{L}^{\theta}_j\right)}_{\text{time variation}} = & \underbrace{\frac{\partial}{\partial x_j}\left\{-C_p\left(\bar{\rho}\tilde{u}_j\tilde{T}\tilde{T} - \hat{\bar{\rho}}\hat{\tilde{u}}_j\hat{\tilde{T}}\hat{\tilde{T}}\right) + 2k\left(\tilde{T}\frac{\partial \tilde{T}}{\partial x_j} - \hat{\tilde{T}}\frac{\partial \hat{\tilde{T}}}{\partial x_j}\right) + 2C_p\left(q_j\tilde{T} - Q_j\hat{\tilde{T}}\right)\right\}}_{\text{redistribution}} \\ & -2\left(\tilde{k}\frac{\partial \tilde{T}}{\partial x_j}\frac{\partial \tilde{T}}{\partial x_j} - \hat{\tilde{k}}\frac{\partial \hat{\tilde{T}}}{\partial x_j}\frac{\partial \hat{\tilde{T}}}{\partial x_j}\right) + 2C_p\left(\overline{q_j\frac{\partial \tilde{T}}{\partial x_j}} - Q_j\frac{\partial \hat{\tilde{T}}}{\partial x_j}\right)\end{aligned} \tag{15}$$

Assuming that time variation and redistribution terms are negligible, a global integration of Eq. (15) results in a dynamic evaluation of Pr_{DVME}:

$$Pr_{DVME} = -\frac{C_p\left\langle \mu_{sgs}\frac{\partial \tilde{T}}{\partial x_j}\frac{\partial \tilde{T}}{\partial x_j} - \mu^t_{sgs}\frac{\partial \hat{\tilde{T}}}{\partial x_j}\frac{\partial \hat{\tilde{T}}}{\partial x_j}\right\rangle_V}{\left\langle \tilde{k}\frac{\partial \tilde{T}}{\partial x_j}\frac{\partial \tilde{T}}{\partial x_j} - \hat{\tilde{k}}\frac{\partial \hat{\tilde{T}}}{\partial x_j}\frac{\partial \hat{\tilde{T}}}{\partial x_j}\right\rangle_V} \tag{16}$$

For convenience, this model is termed DVME in the present article.

Numerical Model

Turbulent natural convective flow is simulated in an enclosed cavity with two differentially heated opposite walls. The geometry is shown in Figure 1 which corresponds to the experimental apparatus used by King (1989) with an aspect ratio of $H/W = 5$. A hot wall ($x = 0$) and a cold wall ($x = W$) were maintained isothermal giving a temperature difference of 45.8°C. No-slip boundary condition is used for the velocities at all solid walls while Dirichlet boundary condition is applied at the hot and cold walls where $T_{Hot} = 77.2$°C and $T_{Cold} = 31.4$°C. This yields a Rayleigh number based on the cavity width as $Ra = 4.56 \times 10^{10}$. For the insulated walls, Neumann boundary condition is applied, i.e. $\partial T/\partial n = 0$, where n is the direction perpendicular to the wall. The predicted temperature field is validated against wall temperatures that have been measured via twenty thermocouples with an accuracy of ±0.2 K. The predicted velocity field is validated against Laser Doppler Anemometer (LDA) measurements with uncertainty of the velocity measurements approximated to be about ±0.02 m/s.

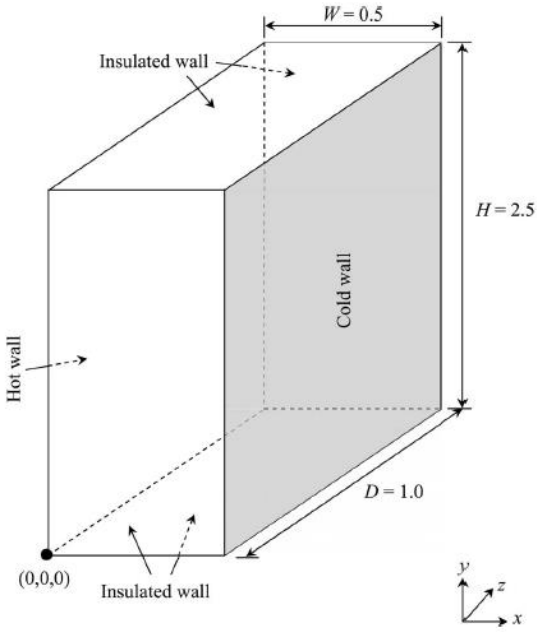

Figure 1. Geometry of the cavity.

Finite volume formulation is utilized to discretize the filtered equations on a collocated grid. The convective terms are approximated using the fourth-order central differencing scheme while the diffusion terms and other spatial derivatives are approximated using the second-order central differencing scheme. The numerical solution is advanced in time using an explicit two-step predictor-corrector approach. It involves a second-order Adams-Bashforth time integration scheme for the predictor stage and a second-order quasi Crank-Nicolson integration scheme for the corrector stage. Pressure correction steps which are incorporated in both the predictor and corrector stages involve the inversion of pressure correction Poisson equations and are solved by means of Krylov methods. Detailed derivation and implementation of the numerical method can be found in Lau et al. (2011).

Three grid resolutions are tested and their details are presented in Table 1 in wall units. From Table 1, it is clear that even the coarse mesh (DVME1) is sufficient to resolve the development of boundary layer in turbulent natural convection since the first mesh point lies within $x^+ < 1.1$,

implying that viscous sublayer of the turbulent boundary layer is sufficiently resolved. It has been found that at least 6 mesh points are allocated in regions close to the wall to sufficiently capture formation of the turbulent structures in the cavity. A non-uniform mesh is applied where further from the walls the grid points are stretched geometrically toward the core of the cavity where the flow is expected to be highly stratified. Differences between the mean velocity profiles in the coarse (DVME1), medium (DVME2) and fine (DVME3) grid resolutions have been found to be small and do not exceed 4.2%. Thus in the following, numerical results are presented for the fine mesh unless mentioned otherwise. All simulations are carried out for approximately 25 000 time steps to allow initial transients to develop in the cavity before data are gathered from additional 100 000 time steps to satisfactorily capture the turbulent statistics. Stability of the numerical algorithm is ensured by employing a maximum Courant–Friedrichs–Lewy (CFL) criterion of 0.35 in all simulations.

Table 1. Mesh Specification of Cases Simulated in Present Study

Case	Grid Points (x,y,z)	x^+	Δy^+	Δz^+
DVME1	(75,163,78)	≤ 1.01	≤ 41	≤ 43
DVME2	(112,204,94)	≤ 0.67	≤ 34	≤ 39
DVME3	(131,245,119)	≤ 0.32	≤ 26	≤ 34

Results and Discussion

For validating the numerical model, Figs. 2 and 3 compare the evolution of time-averaged velocity and mean non-dimensional temperature $\Theta = \left(\tilde{T} - T_{Cold}\right) / \left(T_{Hot} - T_{Cold}\right)$ profiles along the height of the cavity in the central x-y plane. Overall, good agreement is achieved between the predicted and measured profiles. Nevertheless, predicted temperatures are observed to be higher than the experimental data at y/H = 0.5. This discrepancy is consistent with the LES simulations performed by Barhaghi and Davidson (2007) on the same geometry where possibly heat loss could have occur in the experimental apparatus especially in the upper section of the cavity due to the imperfect insulation along the walls.

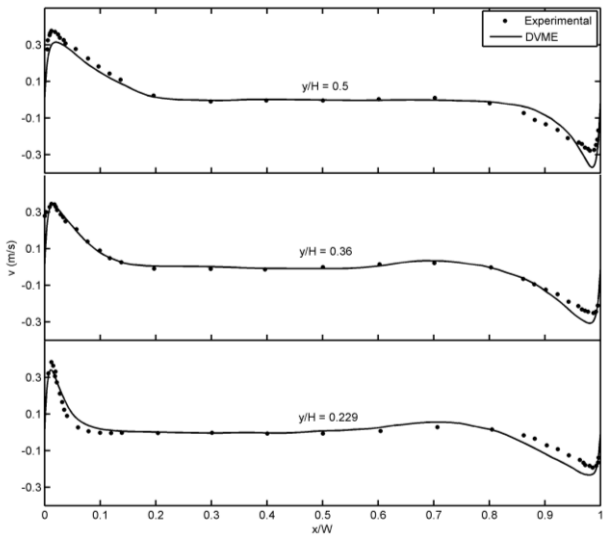

Figure 2. Velocity profiles

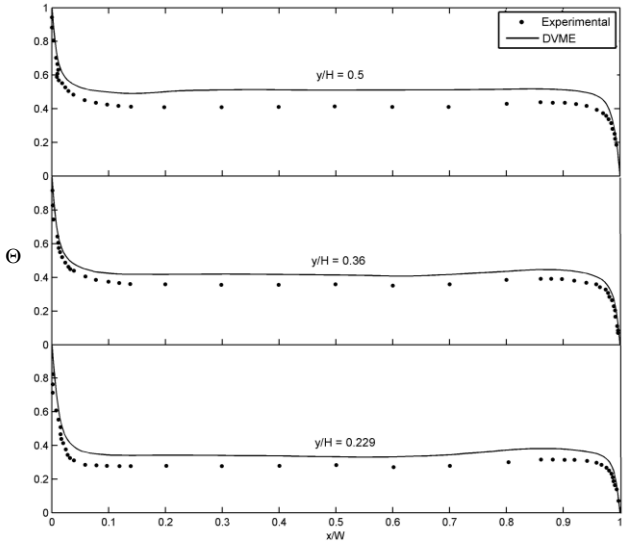

Figure 3. Temperature profiles.

In order to describe the transition phenomena of turbulent natural convective flow in the cavity, the onset of transition is primarily triggered by disturbances which propagate in hook-like structures along the boundary layer in the form of Tollmein-Schlichting waves. Figs. 4 and 5 depict the

formation of coherent structures are represented by iso-surfaces of the *Q*-criterion as was detailed by Hunt et al. (1988) for the hot and cold vertical walls respectively. Flow in the beginning portion of the hot wall is clearly laminar for a shorter period due to the absence of vortices in the height section $0 < y/H < 0.2$. However, the flow in the beginning portion of the cold wall remains rather laminar for a longer period due to the absence of vortices in the height section $0.5 < y/H < 1.0$. As the flow travels upwards along the hot vertical wall and downwards along the cold vertical wall, propagation of Tollmein-Schlichting waves which resemble the characteristic hook-like structures in the instantaneous isotherms ensues as disturbances began to amplify in the boundary layer. This distinctive hook pattern may be recognized as a series of vortex rolls in which faster moving fluid in the inner region of the waves are thrown out into the stratified core, leaving behind a region of lower pressure. As a result, fluid from the exterior whose temperature is lower than that in the inner region is decelerated and thereby entrained toward the wall, triggering a folding mechanism which progresses as the waves propagate. As time proceeds further, vorticity within these structures becomes excessively large that certain segments along a vortex roll starts to lift off from the wall, thereby disrupting the boundary layer and resulting in structures which are mostly irregular and disorganized

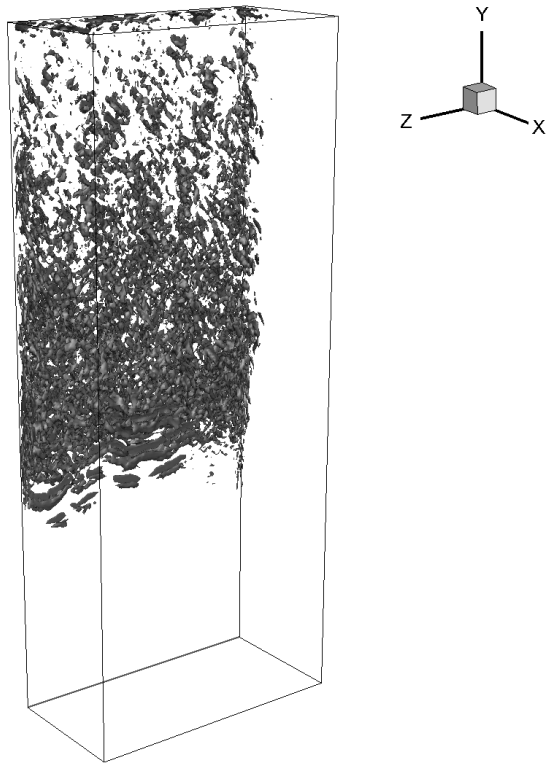

Figure 4. Coherent structures near the hot wall.

Figure 5. Coherent structures near the cold wall.

The transition phenomena due to relaminarization can also co-exist for turbulent natural convective flow in the cavity especially at the corners between hot and top walls and between cold and bottom walls. Figs. 6 and 7 illustrate the instantaneous isotherms of *z*-vorticity accompanied by the velocity vectors of the flow fields near these two regions. It can be clearly seen that the relaminarization behavior of the flow near the top horizontal adiabatic wall is distinctly different from the flow near the bottom horizontal adiabatic wall. Breakdown of coherent structures as the upward flow along the hot vertical wall hits the top horizontal adiabatic wall appears to be more gradual while the downward flow along the cold vertical wall hitting the bottom horizontal adiabatic wall augmented by the gravitational acceleration appears to be more abrupt.

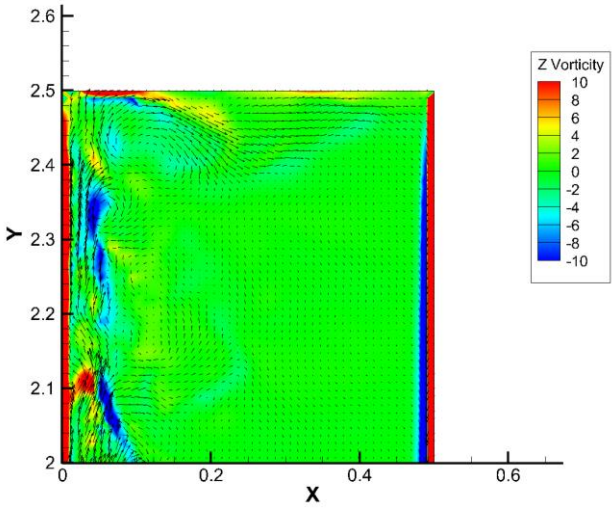

Figure 6. Relaminarization flow structures near the top wall.

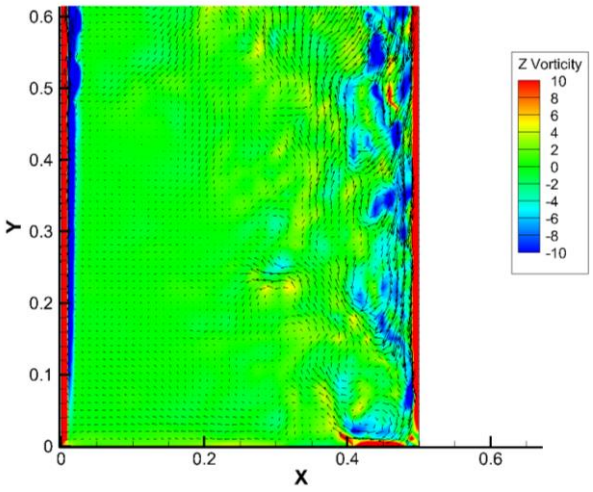

Figure 7. Relaminarization flow structures near the bottom wall.

Conclusions

The dynamic procedure based on "global equilibrium" to determine the model coefficient of the Vreman SGS model in LES is applied to simulate the characteristics of turbulent natural convection in an enclosed cavity. The onset of transition of different flow regimes of the boundary layer is found to be prevalent along the hot and cold vertical walls as well as the flow turns at the top and bottom horizontal adiabatic walls. Essentially, propagation of Tollmein-Schlichting waves recognized as a series of vortex rolls exist along the hot and cold walls. The relaminarization behaviour is characterised by the breaking down of the coherent structures which occurs at the top and bottom horizontal adiabatic walls.

References

Betts, P. L. and Bokhari, I. H. (2000), Experiments on turbulent natural convection in an enclosed tall cavity. *Int. J. Heat Fluid Flow*, 21, pp. 675-683.

Elder, J. W. (1965), Turbulent free convection in a vertical slot. *J. Fluid Mechanics*, 23, pp. 99-111.

Erlebacher, G., Hussaini, M. Y., Speziale, V. G. and Zang, T. A. (1992), Towards the large-eddy simulations of compressible turbulent flows. *J. Fluid Mechanics*, 238, pp. 155-185.

Hunt, J. C. R., Wray, A. A. and Moin, P. (1988), Eddies, streams, and convergence zones in turbulent flows. Proceedings of the Summer Program, Centre for Turbulence Research.

Jaluria, Y. and Gebhart, B. (1977), On disturbance growth mechanisms in a buoyancy induced flow. *Int. J. Heat Mass Transfer*, 20, pp. 434-437.

King, K. J. (1989), Turbulent natural convection in rectangular air cavities. Ph.D. Thesis, Queen Mary College, University of London, London.

Lau, G. E., Yeoh, G. H., Timchenko, V. and Reizes, J. A. (2011), Large-eddy simulation of turbulent natural convection in vertical parallel-plate channels. *Num. Heat Transfer, Part B: Fundamentals*, 59, pp. 259-287.

Lee, J., Choi, H. and Park, N. (2010) Dynamic global model for large eddy simulation of transient flow. *Phys. Fluids*, 22, pp. 125109.

Paolucci, S. and Chenoweth, D. R. (1989), Transition to chaos in a differentially heated vertical cavity. *J. Fluid Mechanics*, 201, pp. 379-410.

Paolucci, S. (1990), Direct numerical simulation of two-dimensional turbulent natural convection in an enclosed cavity. *J. Fluid Mechanics*, 215, pp. 229-262.

Trias, F. X., Soria, M., Oliva, A. and Perez-Segarra, C. D. (2007), Direct numerical simulations of two- and three-dimensional turbulent natural convection flows in a differentially heated cavity of aspect ratio 4. *J. Fluid Mechanics*, 586, pp. 259-293.

You, D. and Moin, P. (2007), A dynamic global-coefficient subgrid-scale eddy-viscosity model for large-eddy simulation in complex geometries. *Phys. Fluids*, 19, pp. 065110.